The Astronomical Journal, 171:165 (14pp), 2026 March https://doi.org/10.3847/1538-3881/ae3c0d

UOCS-XIX. A Multiwavelength Study of Open Cluster Trumpler 5: Cluster Properties and Exotic Populations

Komal Chand[1], Anju Panthi[1,2], and Kaushar Vaidya[1]
[1] Department of Physics, Birla Institute of Technology and Science–Pilani, 333031, Rajasthan, India; p20210463@pilani.bits-pilani.ac.in, p20190413@pilani.bits-pilani.ac.in, kaushar@pilani.bits-pilani.ac.in
[2] Indian Institute of Astrophysics, Koramangala II Block, Bangalore-560034, India
Received 2025 October 3; revised 2026 January 8; accepted 2026 January 20; published 2026 February 17

Abstract

Trumpler 5 is a populous, intermediate-age (∼3 Gyr), metal-poor ([Fe/H] ∼ −0.4) open cluster, located at a distance of approximately ∼3050 pc. This is a well-studied cluster for its broadened main-sequence (MS) and blue straggler star (BSS) population. We present a UV-based analysis of the BSS and blue lurker (BL) candidates of this cluster using AstroSat/UVIT data along with Gaia DR3 data. We use a machine learning-based algorithm, ML-MOC, on Gaia DR3 data, and identify 3150 high-probability ($P > 0.6$) cluster members, along with 305 moderate probability ($0.2 < P < 0.6$) cluster members. Among the cluster members, we identified 32 high-probability BSSs, 13 of which have counterparts in AstroSat/UVIT filters. Additionally, we find 11 MS stars with UVIT counterparts, which we term BL candidates. Upon examining the cumulative radial distribution of various stellar populations, we find the signature of mass segregation in the cluster, with massive stars, including the BSSs and the turnoff stars, found more centrally concentrated than low-mass stars. We investigate the properties of 10 BSS and six BL candidates through multiwavelength spectral energy distributions. We infer the presence of unresolved hot companions in a single BSS and four BL candidates. Our analysis suggests that the hot companion of the BSS is likely a hot subdwarf, whereas the companions of the BL candidates are likely low-mass white dwarfs. We conclude that these five BSS and BL candidates have formed via Case-A/Case-B mass-transfer events, with timescales ranging from ∼26 to 155 Myr.

Unified Astronomy Thesaurus concepts: Open star clusters (1160); Star clusters (1567)

Materials only available in the online version of record: data behind figure

1. Introduction

Open clusters (OCs) are excellent probes for studying stellar evolution and dynamics in a relatively low-density environment (E. D. Friel 2013). These clusters have a wide range of ages, varying from a few million to several billion years; they provide insight into the processes that govern star formation, binary evolution, and cluster dynamics. Binary star interactions are important for understanding the evolutionary pathways of individual stars and the cluster's dynamic stability (H. M. Boffin et al. 2015). Some of the intriguing outcomes of binary interactions in OCs are the formation of blue straggler stars (BSSs, A. Sandage 1953) and blue lurkers (BLs, E. Leiner et al. 2019). BSSs are brighter and bluer than the main-sequence turnoff (MSTO) stars in the color–magnitude diagram (CMD), and hence challenge our understanding of stellar dynamics, mass transfer (MT), and binary interactions. Their positions on the CMD indicate that these are among the most massive population of star clusters (M. M. Shara et al. 1997; F. R. Ferraro & B. Lanzoni 2007; G. Fiorentino et al. 2014). They are believed to have accumulated extra mass through unusual processes, resulting in their rejuvenation and making them appear younger than their counterparts. Due to their relatively higher masses, BSSs are expected to be the most affected by the dynamical friction. In this dynamic process, more massive stars drift toward the cluster's center over time due to energy equipartition. The spatial distribution of BSSs concentrated near the core of a cluster is a key indicator of its dynamical evolution and current relaxed state (M. Aurière et al. 1990; E. Alessandrini et al. 2016).

There are three widely accepted primary mechanisms for the formation of BSSs. (i) Direct stellar collisions. when two or more stars collide in dense environments, they result in the formation of a single BSS (J. Hills & C. Day 1976; P. J. Leonard 1996). (ii) MT through Roche lobe overflow. In binary systems, MT can produce either a single massive BSS or a binary BSS with a companion (W. McCrea 1964). In binaries with a short orbital period ($P < 10$ days), MT takes place when the primary is still in the MS (Case A, R. F. Webbink 1976). Such a system can undergo a complete merger, producing a single massive BSS, or can produce a binary BSS with a short-period MS companion. In binary systems with $P \sim$ 10–300 days, MT occurs when the primary is in the red giant branch (RGB) phase, leaving behind a BSS with a helium-core (He) white dwarf (WD) with a mass $\leqslant 0.45\ M_{\odot}$ as a companion (Case B, W. McCrea 1964). For binary systems with $P \sim$ 300–3000 days, MT occurs when the primary is in the asymptotic giant branch (AGB) phase, producing a long-period binary BSS with a carbon–oxygen (CO) WD with a mass $\sim 0.5\ M_{\odot}$ as a companion (Case C, X. Chen & Z. Han 2008). For binaries with even longer orbital periods, MT can happen via wind Roche lobe overflow during the AGB phase, resulting in a wide, long-period binary BSS with a CO WD companion (Case D, A. M. Geller & R. D. Mathieu 2011). (iii) Origin in hierarchical triple stars. The Kozai mechanism combined with tidal friction can induce

Table 1
Fundamental Parameters of Trumpler 5 from the Literature

Parameter	Value	Reference(s)
Age (Gyr)	3–4.6	A. E. Piatti et al. (2004), M. J. Rain et al. (2021), K. K. Rao et al. (2023), F. Lucertini et al. (2023)
Radius (arcmin)	20	K. K. Rao et al. (2023)
Distance (pc)	2400–3190	A. E. Piatti et al. (2004), M. J. Rain et al. (2021), K. K. Rao et al. (2023)
[Fe/H] (dex)	−0.4	A. E. Piatti et al. (2004), M. J. Rain et al. (2021), F. Lucertini et al. (2023)
$E(B-V)$ (mag)	0.58–0.62	A. E. Piatti et al. (2004), M. J. Rain et al. (2021), F. Lucertini et al. (2023)

the formation of a close inner binary in a hierarchical triple system. Subsequent angular momentum loss through stellar evolution or magnetic braking can trigger MT or a merger between the components, resulting in the formation of a binary BSS or a single massive BSS (H. B. Perets & D. C. Fabrycky 2009). Another intriguing outcome of binary interaction is the formation of BLs. These stars are rejuvenated by MT, mergers, or collisions, similar to BSSs, but conversely, they are fainter than the MSTO stars (E. Leiner et al. 2019). In some cases, the amount of accreted material is insufficient; in others, the accreting stars are relatively smaller, therefore the progenitor does not outshine the stars at the MSTO and fall into a category of BLs. In several instances, these stars are indistinguishable from the MS or MSTO stars in most ways, except that they have higher rotational velocities ($v\sin i$) or exhibit excess at ultraviolet (UV) wavelengths. Some of the techniques to identify BLs are detection of increased rotation, unusual chemical signatures, or the presence of a companion (V. V. Jadhav et al. 2019; A. Panthi et al. 2024). So far, 11 BLs have been detected in the old OC M67 (V. V. Jadhav et al. 2019) and in NGC 6940 (A. Panthi & K. Vaidya 2024) using the AstroSat/UVIT (P. C. Agrawal 2017) data.

Trumpler 5 is an intermediate-age OC with an estimated age of ∼3 Gyr (M. J. Rain et al. 2021). Its fundamental parameters, such as age, distance, reddening, and metallicity, have been determined through various spectroscopic and photometric studies and are listed in Table 1. Trumpler 5 is known to be affected by significant differential reddening (DR), which can introduce uncertainties in the determination of its fundamental parameters and stellar properties. Dust in star clusters significantly influences the observed properties of stellar populations (L. P. Cassarà et al. 2013). Dust along the line of sight can cause reddening and extinction, affecting optical and UV magnitudes. As a result, it complicates the detection and characterization of BSSs, BLs, and their hot companions (M. J. Rain et al. 2021). In particular, DR arises from spatial variations in dust distribution across the cluster field, leading to varying levels of extinction along different lines of sight. This effect can significantly distort the CMD, making it essential to correct for accurate stellar population studies (A. P. Milone et al. 2012). Several studies have shown that clusters with significant reddening require extinction correction for differential absorption effects (D. Massari et al. 2012; M. J. Rain et al. 2021). Despite the challenges posed by dust, UV observations play a crucial role in identifying hot companions by detecting UV excess. Several studies have been done to identify hot companions in OCs using UV data. For instance, N. M. Gosnell et al. (2015) used Hubble Space Telescope data to identify WD companions among BSSs in NGC 188. Similarly, hot companions for exotic populations are identified using AstroSat/UVIT observations (A. Subramaniam et al. 2016, N. Sindhu et al. 2018; V. V. Jadhav et al. 2021; A. Panthi et al. 2022, 2024; K. Vaidya et al. 2022) as well as Swift/UVOT observations (K. K. Rao et al. 2022; K. Chand et al. 2024). Although previous studies have identified BSSs in Trumpler 5 (M. J. Rain et al. 2021; K. K. Rao et al. 2021), neither their properties nor their formation mechanisms have been studied using UV data. Moreover, no previous study on the cluster has searched for BL candidates in this cluster. This work presents the first detailed UV-guided multiwavelength study using observations from AstroSat/UVIT. Additionally, we examine the spatial distribution of various stellar populations to investigate mass segregation to assess whether the cluster has undergone dynamical evolution.

The paper is organized as follows. In Section 2, we describe the observational data, the data reduction procedures, and the archival datasets used in this study. In Section 3, we present our analysis and results, including membership identification, CMD construction, differential reddening, mass segregation analysis, and spectral energy distributions (SEDs). Section 4 discusses the implications of our findings. Finally, Section 5 summarizes our conclusions.

2. Observational Data and Data Reduction

Our study makes use of the UV observations carried out with the UVIT on board the AstroSat telescope, Gaia DR3 observations, and other archival observations spanning the long wavelength range from the far-UV to mid-IR, which are detailed below.

2.1. UVIT Data and Data Reduction

AstroSat is India's first space-based observatory for multi-wavelength astronomy and was launched on 2015 September 28. The Ultraviolet Imaging Telescope (UVIT) is one of the payloads on board AstroSat. It operates in three channels (K. P. Singh et al. 2014): far-ultraviolet (FUV; 130–180 nm), near-ultraviolet (NUV; 200–300 nm), and visible (VIS; 350–550 nm). The FUV and NUV channels are mainly utilized for scientific observations, while the VIS channel is primarily used for correcting spacecraft drift. Comprehensive information about UVIT's calibration and instrumentation is given by A. Kumar et al. (2012) and S. N. Tandon et al. (2017). Trumpler 5 was observed with AstroSat/UVIT on 2023 April 21, under proposal ID A12_097T02_9000005542. Observations were carried out in three FUV filters: F148W (1481 ± 250 Å), F154W (1541 ± 190 Å), and F169M (1608 ± 145 Å) with exposure times of 1726 s, 7340 s, and 534 s respectively. Due to the relatively short exposure time in the F169M filter and the resulting large errors in flux measurements, we have excluded this filter from our study. Table 2 presents details on observational exposure time, the number of sources observed in the FUV filters, and the number of ML-MOC cluster members detected as FUV counterparts.

Table 2
UVIT Observations

Filter Name	Exposure Time (s)	Total UVIT Detections	ML-MOC Members in UVIT
F148W	1726	1172	7
F154W	7340	1265	20

We utilized UVIT data and processed them using the CCDLAB software (J. E. Postma & D. Leahy 2017) to generate science-ready images. This included standard calibration such as correction for flat-fields, geometric distortion, and spacecraft drift. For a detailed description of the UVIT instrument, its in-orbit performance, and calibration procedures, we refer the reader to A. Kumar et al. (2012) and S. N. Tandon et al. (2017). The final science-ready images in F148W and F154W filters were well studied for photometric analysis. To obtain accurate stellar photometry, we used the point-spread function (PSF) fitting technique available in the DAOPHOT package in IRAF (P. B. Stetson 1987). This process involved source detection above a threshold determined from the background, generating a PSF model using isolated stars, and iterative fitting of this PSF to all identified sources. The resulting PSF magnitudes were converted to the AB magnitude system using the zero-point values provided by S. N. Tandon et al. (2020). Additionally, aperture corrections based on curve-of-growth analysis were applied to ensure consistency between aperture and PSF photometry. We also implemented saturation corrections following S. N. Tandon et al. (2020) to account for high photon incidence rates.

2.2. Archival Data

To study the physical properties of the detected stars, we combined UVIT observations with multiple other wavelengths. Along with AstroSat/UVIT data, we utilized Galaxy Evolution Explorer (GALEX) data for UV wavelengths. GALEX (D. C. Martin et al. 2005) is a space-based telescope that operates in two UV bands: FUV (1350–1780 Å) and NUV (1770–2730 Å). For Trumpler 5, flux measurements in GALEX are available in the NUV regime only. Optical data are obtained from Gaia (A. Vallenari et al. 2023) and Panoramic Survey Telescope and Rapid Response System (Pan-STARRS; E. Schlafly et al. 2012). Gaia provides measurements of parallaxes, proper motions, stellar positions, and kinematics for more than a billion stars. It also provides photometry in three filters (C. Jordi et al. 2010): G (6230 ± 2092 Å), G_{BP} (5050 ± 1172 Å), and G_{RP} (7730 ± 1378 Å). In addition, Pan-STARRS (E. Schlafly et al. 2012; J. Tonry et al. 2012) provides imaging through five optical bands: g (4810 ± 687 Å), r (6170 ± 701 Å), i (7250 ± 649 Å), z (8660 ± 522 Å), and y (9620 ± 414 Å). The IR data are taken from the Two-Micron All-Sky Survey (2MASS; M. Cohen et al. 2003) and Wide-field Infrared Survey Explorer (WISE; E. L. Wright et al. 2010). 2MASS operates in three near-IR regions: J (12350 ± 812 Å), H (16620 ± 1254 Å), and K_s (21590 ± 1309 Å). WISE is a space-based observatory that extends coverage into four mid-IR bands: W1 (33526 ± 3313 Å), W2 (46028 ± 5211 Å), W3 (115608 ± 27528 Å), and W4 (220883.00 ± 20500 Å).

3. Analysis and Results

3.1. Membership Identification

Accurate identification of cluster members is essential in studying OCs, as the presence of field stars can significantly affect the analysis. We used a machine learning-based algorithm, ML-MOC (M. Agarwal et al. 2021), to achieve reliable membership determination. This algorithm utilizes Gaia astrometric and photometric data to identify cluster members and combines two key techniques: k-nearest neighbour (kNN, T. Cover & P. Hart 1967) for initial filtering of field stars and Gaussian mixture model (D. Peel & G. J. McLachlan 2000) for probabilistic classification. We begin by selecting all Gaia sources within 40′ radius of the cluster center that have complete astrometric data (R.A., decl., proper motion in R.A. and decl., and parallax), valid Gaia magnitudes (G, G_{BP}, G_{RP}), non-negative parallaxes, and G-band errors less than 0.005 mag. Stars with membership probabilities greater than 0.6 are considered reliable members, while those with probabilities between 0.2 and 0.6 are also included to ensure the completeness of the final member catalog. We refer the reader to M. Agarwal et al. (2021) for a comprehensive explanation of the ML-MOC algorithm. We identified 3149 sources with cluster membership probabilities $\geqslant$0.6 and an additional 305 sources with probabilities between 0.2 and 0.6. By plotting the radial distribution of the identified members, we estimate the cluster radius to be 20′, beyond which the stellar density is found to merge with the average field density. This value is consistent with the radius previously reported by K. K. Rao et al. (2023). Figure 1 presents the distributions of spatial coordinates, proper motion, and parallax for the sample sources and the identified cluster members.

3.2. The Color–Magnitude Diagram

CMDs are fundamental tools used to analyze different evolutionary phases of stars within a cluster. The observed optical CMD for cluster members obtained using the ML-MOC algorithm is shown in Figure 2 with a PARSEC isochrone (A. Bressan et al. 2012) of age 3 Gyr (K. K. Rao et al. 2023) and metallicity of $[Fe/H] = -0.40$ (M. J. Rain et al. 2021) overplotted on it. The CMD shows a broadened main sequence with a clear gap near the main-sequence turnoff, and an elongated red clump with the elongation approximately parallel to the direction of interstellar reddening. To address this issue of DR, we applied DR correction across the cluster (refer to Section 3.3), which helps to recover a cleaner and more accurate CMD.

3.3. Differential Reddening

The nonuniform distribution of interstellar dust, commonly known as DR, often affects star clusters. It can significantly impact the appearance of the CMD, such as by broadening the MS, subgiant branch, and RGB. If left uncorrected, DR can lead to incorrect determination of fundamental cluster parameters such as age, distance, and metallicity (I. Platais et al. 2012) as well as misidentification of various stellar populations of the cluster. In the case of OC Trumpler 5, the visibly broadened MS and elongated red clump in the CMD (Figure 3(a)) indicate the presence of differences in the properties of interstellar dust and highlight the necessity for

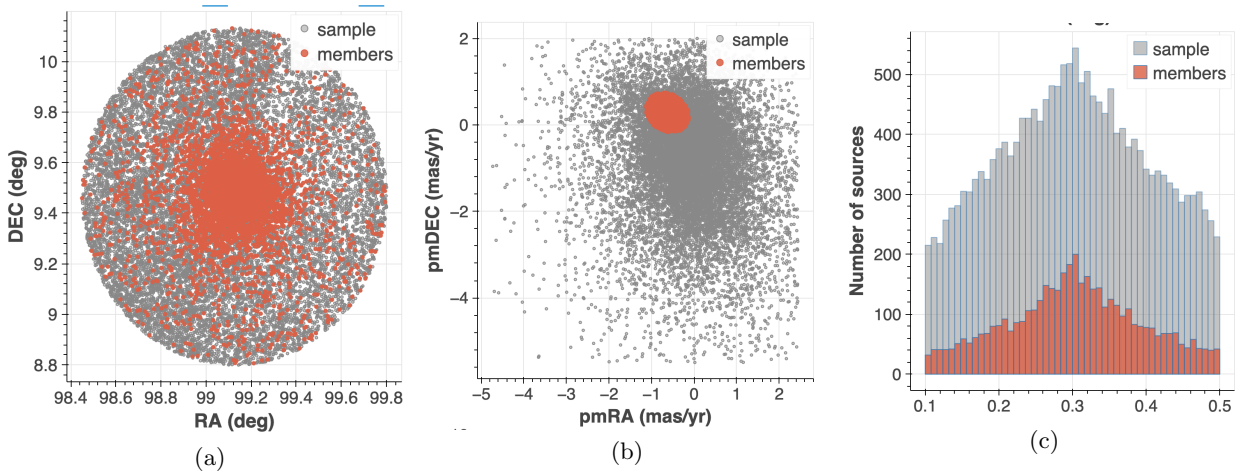

Figure 1. (a) The spatial distribution, (b) proper motion distribution, and (c) parallax distribution of cluster members and sample sources determined using the ML-MOC algorithm on Gaia DR3 data. The Gaia source information and ML-MOC algorithm-derived membership probabilities are available as the data behind the Figure.

(The data used to create this figure are available in the online article.)

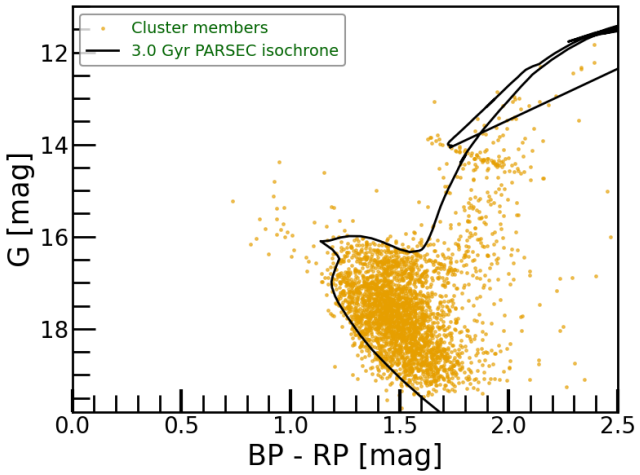

Figure 2. CMD of the cluster members identified using the ML-MOC algorithm on Gaia DR3 data. Orange dots represent high-probability cluster members with the 3 Gyr PARSEC isochrone.

DR correction. Previous studies by M. J. Rain et al. (2021) and K. K. Rao et al. (2023) have implemented such corrections for this cluster. In this work, we follow a similar approach to that adopted by K. K. Rao et al. (2023) using our own set of cluster parameters as per the method briefly explained as follows. First, the cluster distance is calculated using the mean distances for relatively bright ($G < 16$) members using the catalog of C. Bailer-Jones et al. (2021) and a distance, 3050 pc, is obtained for the cluster. Next, the extinction in the G band, $A_G = 1.3$, is determined by taking a median value of A_G for cluster members using Gaia DR3 datasets. Using the extinction relations provided by S. Wang & X. Chen (2019), the corresponding A_V and $E(\mathrm{BP}-\mathrm{RP})$ are computed using the reddening vector, $R_G = A_G/E(\mathrm{BP}-\mathrm{RP})$, where R_G is 1.81. This reddening vector closely aligns with the observed elongation of the red clump, validating its applicability for correction. For reddening corrections, we focus exclusively on MS stars. A grid is constructed over the MS region in the CMD (Figure 3(a)), with the top edge oriented in the direction of the reddening vector, the bottom edge corresponding to the faintest G-mag, and the lateral edges enclosing the full width of the MS. For each cluster member, we use the kNN algorithm to identify 25 nearest neighbors in spatial coordinates. We then examine the individual CMD for these neighboring stars and compute mean BP − RP color and G-mag for stars lying within the grid. The displacement required to shift this mean point onto the isochrone in the direction of the reddening vector is then calculated, providing an estimate of the local reddening and extinction for that member. These individual shifts are used to correct the observed magnitudes and colors for each star within the grid. The corrected CMD (Figure 3(b)) shows a significantly narrower MSTO and red clump region, resulting in a much cleaner and well-defined CMD. Furthermore, the gap near the MSTO is no longer visible in the corrected CMD, indicating the effectiveness of the correction in improving the CMD.

The reddening map of Trumpler 5 is shown in Figure 3(c). The DR map reveals significant spatial variations in extinction across the cluster field. The color excess $E(\mathrm{BP}-\mathrm{RP})$ ranges from ∼0.68 to 1.25 mag. The peripheral regions of the cluster appear relatively uniform in extinction, with the exception of a slightly enhanced extinction patch to the northeast. A prominent high-extinction region is observed to the southwest of the cluster center. The corresponding extinction in the visual band (A_V) ranges from 1.49 to 2.75 mag. This value of visual extinction amounts to an extinction of 3.96–6.05 mag in the UV. We identify 32 high-probability BSSs based on the corrected CMD (Figure 3(b)), adopting the criterion G-mag < (MSTO mag + 0.5) and (BP − RP) < (MSTO mag − 0.2). Among these 32 BSS candidates, 13 have counterparts in AstroSat/UVIT observations. All 13 BSS candidates are detected in the F154W filter, and three of them have counterparts in both F148W and F154W filters. A total of 11 MS stars are detected in UVIT filters, F148W and F154W, and called BL candidates hereafter. The BSS and BL candidates are marked as red stars and magenta open circles, respectively, in Figure 3(b). Additionally, a BSS known as an eclipsing binary in the Gaia DR2 catalog, BSS4, is marked as a yellow dot. The spatial distribution of the BSS and BL candidates is shown on the reddening map in Figure 3(c). The 13 BSS candidates with UVIT counterparts are shown as red stars on the reddening map (Figure 3(c)), whereas the 19 BSS

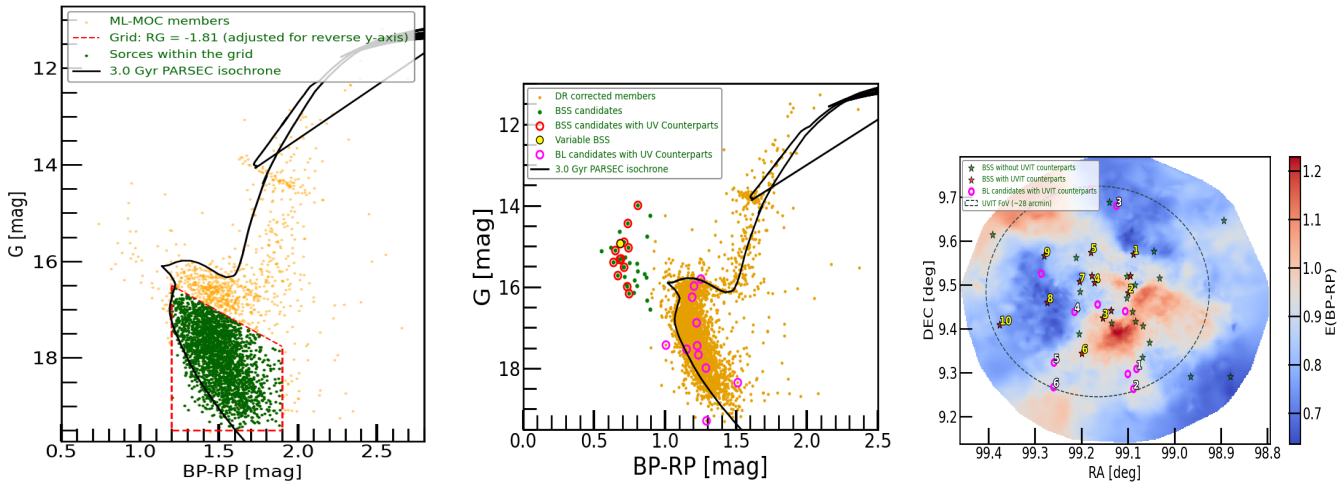

(a) (b) (c)

Figure 3. (a) The selection box for the cluster members used to compute the DR correction is indicated by the red dashed lines. The sources used to estimate the DR are marked as green dots. (b) The corrected CMD after applying DR corrections. Orange dots represent high-probability cluster members, green dots represent BSS candidates identified using ML-MOC, red open circles highlight BSS candidates with UVIT counterparts, and magenta open circles mark BL candidates with UVIT counterparts. The yellow dot marks the variable BSS candidate (BSS4). (c) DR map of the OC Trumpler 5 with the positions of BSS and BL candidates marked on it. The meanings of the symbols and colors are indicated in the legend within the figure.

candidates without UV counterparts are marked as green stars on the reddening map. As can be seen, several BSS candidates lie outside the UVIT field of view. Additionally, many BSSs within the field of view are not detected due to factors such as dust extinction, UV sensitivity, etc. In this study, we analyze 10 of the 13 BSS candidates and six of the 11 BL candidates with UVIT counterparts with no nearby ($<3''$) contaminants. The remaining three BSSs and five BL candidates are excluded from this study due to the lack of IR photometric data. The selected 10 BSS and six BL candidates are additionally marked with their numbers on Figure 3(c).

M. J. Rain et al. (2021) reported a total of 40 BSS candidates in Trumpler 5, whereas K. K. Rao et al. (2021) identified 35 BSSs. Our BSS candidates match more closely to the BSS candidates of K. K. Rao et al. (2021). The significant difference in the numbers of BSSs as compared to those of M. J. Rain et al. (2021) likely arises from differences in cluster membership, DR correction, and BSS selection criteria. The BSS candidates in our study are selected based on a more conservative criterion. The G-mag of these selected BSS candidates ranges from $\sim$13.8 to $\sim$16.2 mag (refer to Figure 3(b)).

3.4. Mass Segregation

Mass segregation is a fundamental dynamical phenomenon in star clusters whereby more massive stars tend to move toward the cluster center. In contrast, low-mass stars tend to move to the outer regions. This process arises due to gravitational interactions among cluster members (G. Meylan & D. C. Heggie 1997). To explore mass segregation in Trumpler 5, we analyze the spatial distribution of different stellar populations. First of all, to select the low-mass population, we checked the 90% completeness limit for the G-mag of T. Cantat-Gaudin et al. (2023). Since the 90% completeness occurs at G-mag $\sim$ 18.4 for this line of sight, we selected members with G-mag ranging between 17 and 18.4 mag as low-mass members. This cutoff at 18.4 mag is adopted to ensure that our mass segregation analysis is not affected by the differences in the level of completeness among the various stellar populations. In addition to this, we chose the MSTO stars (stars with G-mag $\pm$0.2 compared to the turnoff), RGB stars, and the ML-MOC BSS candidates for this analysis. Figure 4 presents the cumulative radial distribution for these four populations. The BSS, RGB, and MSTO stars are found to be significantly more segregated than the low-mass stars, indicating that massive stars are more centrally concentrated. However, the separation between low-mass stars and the massive populations are clearly visible up to $r/r_c \sim 2.5$. Moreover, among the massive populations, the BSS, RGB, and MSTO stars show similar levels of segregation. This suggests that massive populations have not yet developed strong differential segregation among themselves. So we conclude that even though the cluster shows the sign of mass segregation, it is still undergoing dynamical evolution.

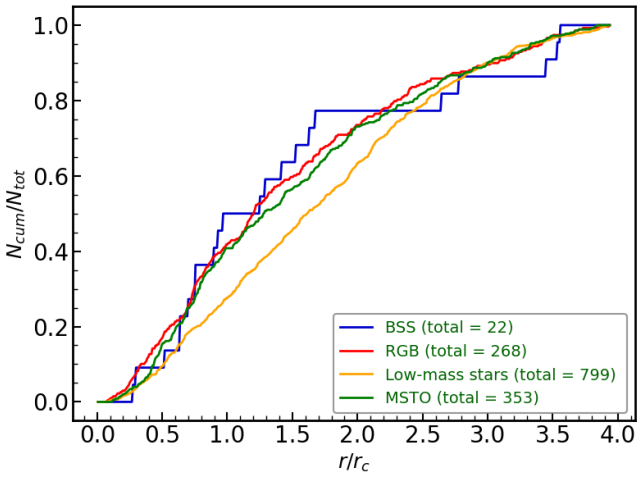

Figure 4. The cumulative radial distributions of the BSS candidates, RGB stars, MSTO stars, and low-mass single stars, with the y-axis representing the normalized fraction of each population and the x-axis indicating the radial distance, expressed in units of the core radius (r_c) of the cluster.

3.5. Spectral Energy Distributions

In order to search for unresolved hot companions and to estimate the fundamental parameters such as the temperature, radius, and luminosity, of the BSS and BL candidates, we constructed their SEDs. Before performing SED analysis, we used Aladin[3] interface to examine each BSS and BL candidate for nearby sources of contamination within a 3″ radius. For all the 10 BSS and six BL candidates, no nearby sources were found within the 3″ radius, ensuring they are well isolated and suitable for reliable SED fitting. The SEDs are generated using Virtual Observatory SED Analyzer (VOSA; A. Bayo et al. 2008), which compiles photometric data for multiple wavelength ranges. Then the observed fluxes are corrected using the extinction law of E. L. Fitzpatrick (1999) and R. Indebetouw et al. (2005). VOSA computes synthetic photometry by applying filter transmission curves to selected theoretical models. The best-fit model is determined by a χ^2 minimization process and is given by the following formula:

$$\chi_r^2 = \frac{1}{N - N_f} \sum_{i=1}^{N} \frac{(F_{o,i} - M_d F_{m,i})^2}{\sigma_{o,i}^2}. \quad (1)$$

In the above equation, N is the total number of photometric data points, N_f represents the total number of fitted model parameters, $F_{o,i}$ denotes the observed flux, $F_{m,i}$ is the model flux of the star, $\sigma_{o,i}$ is the error associated with the observed flux, and $M_d = (R/D)^2$ is the scaling factor, dependent on the radius and the distance of objects.

To determine the fundamental parameters of all the BSS and BL candidates, we utilized Kurucz stellar models (F. Castelli et al. 1997) for fitting the SEDs. The parameters defined in VOSA for the fitting process were: temperature range: 3500–50,000 K; surface gravities (log g): 3.0 to 5.0; and metallicity [Fe/H] = −0.5, which closely matches with the cluster's metallicity of −0.40 reported by M. J. Rain et al. (2021). Additionally, we provide a cluster distance of 3050 pc, which is calculated using the mean distances of relatively bright members (G-mag > 18) from the catalog of C. Bailer-Jones et al. (2021). To account for DR, which affects each source differently, we used individual extinction values (A_V) for each BSS candidate and BL candidate, as indicated in Figure 3(c). Our estimated extinction values match closely with the extinction values from the 3D dust maps, presented by G. M. Green et al. (2019), with the maximum difference found to be ±0.3 mag. While fitting the SEDs, to obtain reliable estimates of UV excess, we initially excluded UV data points to check the consistency of optical to IR fluxes with a single stellar component. A small number of optical and IR data points are excluded from the SED fits as these measurements are likely affected by crowding, inconsistencies in photometric calibration, or flagged as low-quality in the respective surveys. Including such contaminated or uncertain fluxes could bias the derived stellar parameters. We then evaluated excess emission in UV flux for each source, which could indicate the presence of a hotter companion. Sources exhibiting a fractional residual in UV excess less than 0.5 were considered for a single-component fit, while sources with fractional residual greater than 0.5 were considered for a binary-component fit. We perform binary SED fitting using a Python-based code by V. V. Jadhav et al. (2021), which employs a χ^2 minimization technique to identify the best-fitting model parameters.

Nine BSS candidates exhibit a fractional residual less than 0.5 and are reasonably well fitted with a single-component SED, as shown in Figure 5. The remaining BSS candidate (BSS3) and six BL candidates exhibit a fractional residual greater than 0.5, indicating a significant UV excess. The excess may arise due to the presence of a hot companion, chromospheric activity such as hot spots in contact or semidetached binaries, high-temperature coronal emission, subluminous companions, magnetic activity, stellar flares, or active binary systems. To investigate the origin of this UV excess, we first searched for X-ray counterparts of these sources. However, no X-ray observations are available for this cluster in either the Chandra or XMM-Newton archives. To explore the possibility that the UV excess is due to an unresolved hot companion, we performed binary-component SED fitting using Kurucz models (F. Castelli et al. 1997). BSS3 was successfully fitted with a binary-component SED, as shown in Figure 6, indicating the presence of a hot companion with an effective temperature of $31{,}000^{+3000}_{-1000}$ K, a radius of $0.05 \pm 0.01\ R_\odot$, and a luminosity of $0.06 \pm 0.02\ L_\odot$. Among the BL candidates, no successful binary-component fits were found for BL1 and BL6, therefore we present only their single SED fits shown in Figure 7. The four BL candidates fitted with binary components are shown in Figure 8. For BL3 and BL5, the fractional residual does not become zero but is noticeably reduced. The best-fit binary SED models of the four BL candidates suggest the presence of hot companions with effective temperatures of 31,000–39,000 K, estimated radii of 0.03–0.06 $R_\odot$, and luminosities of 1.08–6.76 $L_\odot$. Furthermore, UV fluxes from GALEX are available for eight BSSs (refer to Table 3); however, these measurements are excluded from the fitting and are only displayed in the SED plots for reference. We present the observed fluxes of all BSSs in Table 3 and those for BL candidates in Table 4. The estimated parameters for all BSS and BL candidates are listed in Table 5.

4. Discussion and Summary

Trumpler 5 is an intermediate-age, metal-poor OC located in the Galactic anticenter direction. It exhibits a well-populated but significantly broadened MS and an extended red clump in the CMD. Additionally, its diverse stellar populations include a sizable number of BSSs for an OC, products of alternative stellar evolutionary pathways that can provide important clues regarding binary interactions and MT. The cluster is known to suffer significantly from the issue of DR. In addition to a broadened MS and extended red clump, the cluster's CMD also shows a distinct gap just below the MSTO. We study the cluster properties and its dynamical state using its diverse populations, and use a UV-guided approach to investigate the BSSs of the cluster to understand their possible formation mechanisms. The DR map constructed using Gaia photometry reveals notable spatial variations in extinction, with the highest extinction seen toward the southwest region of the cluster. The color excess, $E(\mathrm{BP} - \mathrm{RP})$, ranges from 0.68 to 1.25 mag, corresponding to an extinction of 3.96–6.05 in the FUV filter F154W. The overall variations in the reddening and extinction across the cluster that we found are consistent with the results of K. K. Rao et al. (2023) and M. J. Rain et al. (2021). We observe that the DR correction is effective in significantly narrowing down the extent of the red clump and the width of

[3] https://aladin.cds.unistra.fr/

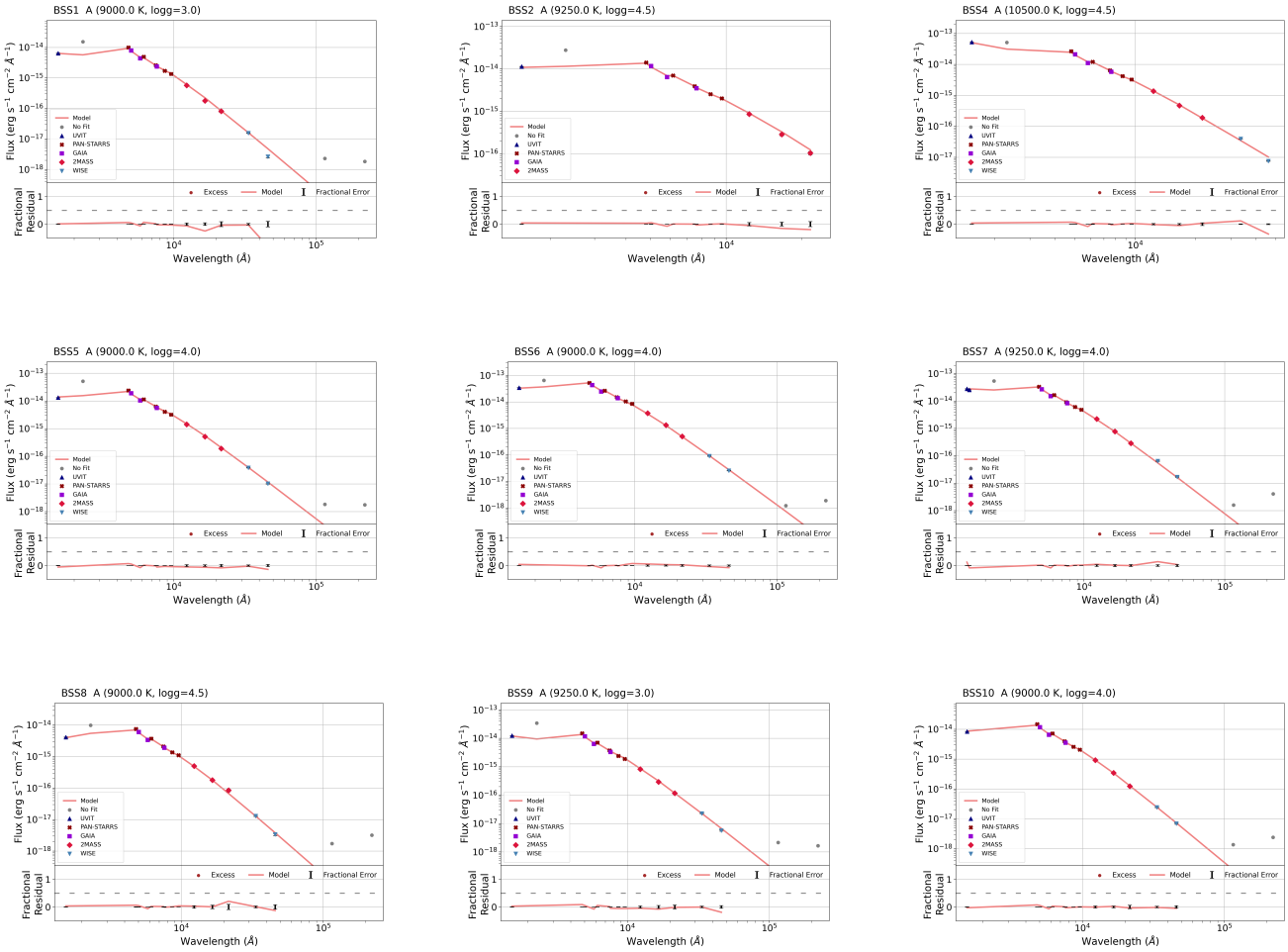

Figure 5. The single-component SED fits for BSS candidates with fractional residuals less than 0.5. In each panel, the upper part displays the extinction-corrected observed fluxes, represented by different shapes and colors corresponding to various filters, with black error bars indicating the associated uncertainties. The red curve denotes the best-fit Kurucz stellar model. The lower part shows the residuals, calculated as the difference between the extinction-corrected observed fluxes and the model fluxes, across filters ranging from UV to IR. Data points shown in gray were excluded from the fitting process.

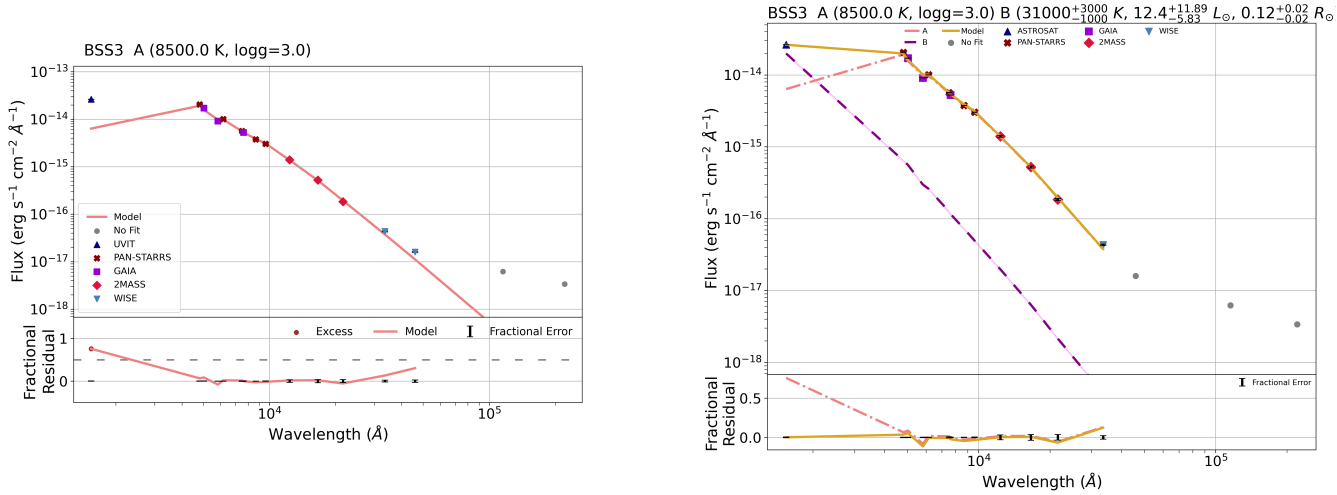

Figure 6. The left panel shows the single-component SED fit of BSS3, plotting the excess in UV flux $> 50\%$, and the right panel shows the binary-component SED of BSS3. The extinction-corrected observed fluxes are shown by different colors for several telescopes as per the legend, with black error bars indicating the corresponding flux uncertainties. The best-fitting cool (A) component is represented by a pink dashed curve, while the hot (B) component is shown by a purple dashed curve. The combined model SED is plotted as an orange curve (labeled Model). Gray data points indicate photometric measurements that were excluded from the fitting process (labeled No fit).

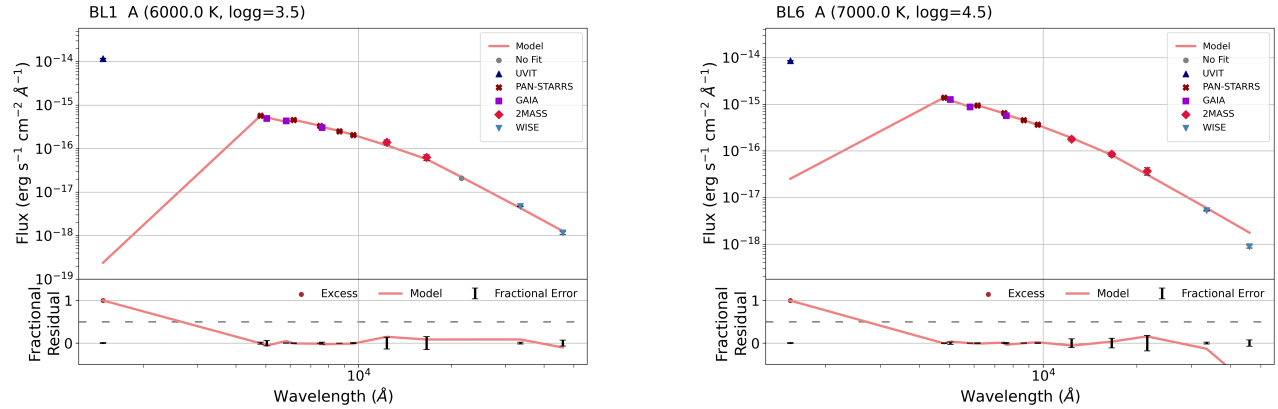

Figure 7. The single-component SED fits for BL1 (left panel) and BL6 (right panel) candidates with fractional residuals greater than 0.5. The symbols and curves mean the same as in Figure 5.

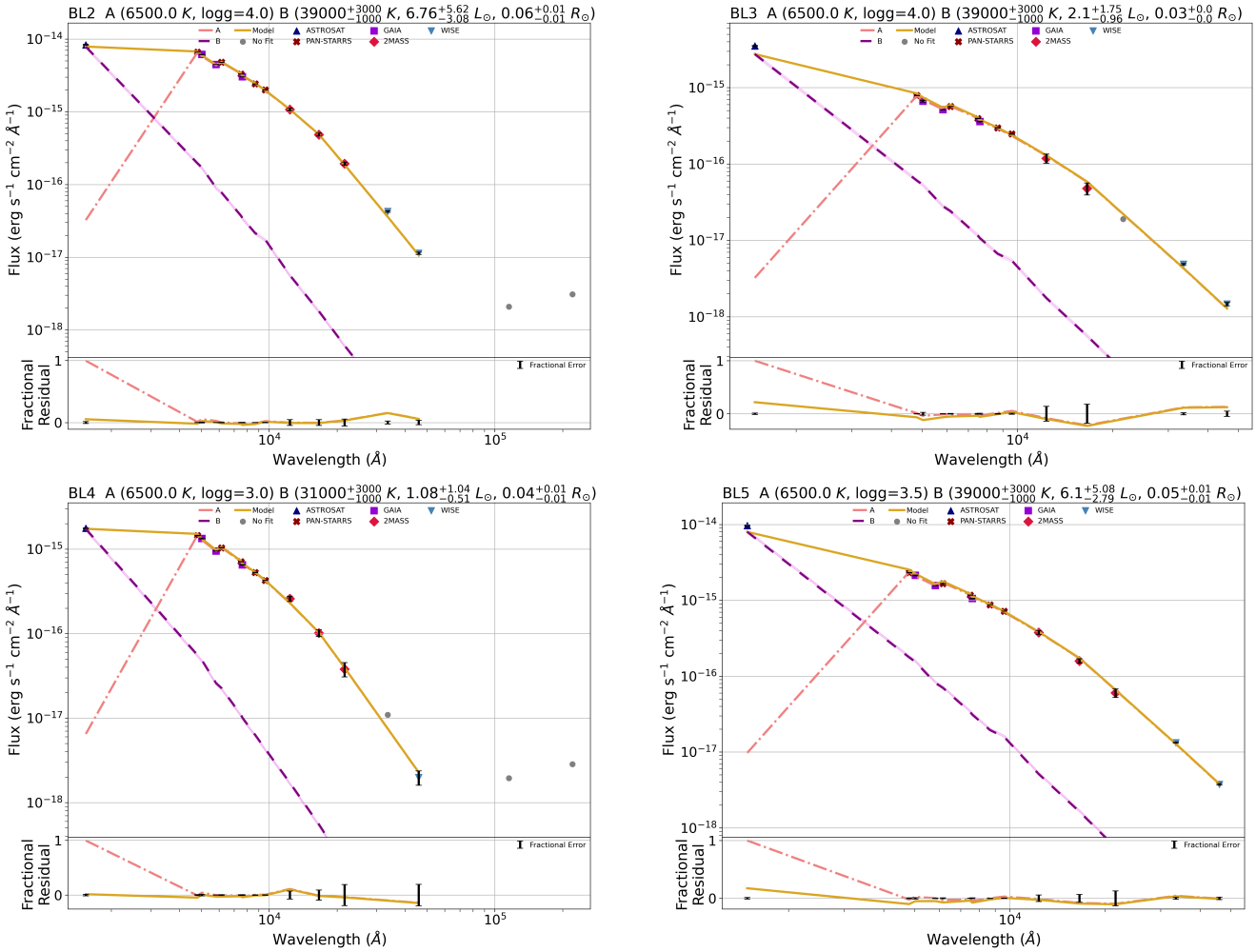

Figure 8. The binary-component SED fits for BL2, BL3, BL4, and BL5. The symbols and curves mean the same as in Figures 5 and 6.

the MS, leading to a cleaner CMD (refer to Figure 3(b)). This correction also removes the gap present near the MSTO in the uncorrected CMD and allows for accurate identification of stellar evolutionary features and population analysis. We identify 3150 high-probability ($P > 0.6$) and 305 moderate-probability ($0.2 < P < 0.6$) cluster members using the ML-MOC algorithm on Gaia DR3 data. For comparison, within a 20′ radius of Trumpler 5, the E. L. Hunt & S. Reffert (2023) catalog lists 3458 members, out of which 3127 members cross-matched with our high-probability cluster members. This indicates a strong consistency between our members and the E. L. Hunt & S. Reffert (2023) members. We then explore the UV properties of cluster members; out of the 32 high-probability BSS candidates, we have only 13 with FUV counterparts, even though 29 are within the UVIT field, which is likely due to the high extinction toward the cluster.

Table 3
Source IDs from Gaia DR3, along with the Coordinates, Flux Values, and Associated Flux Errors for the Stars across All Utilized Filters

Name	GAIA DR3 source_id GAIA3.Gbp ± err PS1.z ± err WISE.W2 ± err	R.A.(J2000) GAIA3.G ± err PS1.y ± err	Decl.(J2000) GAIA3.Grp ± err 2MASS.J ± err	F148W ± err PS1.g ± err 2MASS.H ± err	F154W ± err PS1.r ± err 2MASS.Ks ± err	GALEX.NUV ± err PS1.i ± err WISE.W1 ± err
BSS1	3326834736377867264 1.138e−15 ± 3.85e−18 6.680e−16 ± 3.04e−18 2.406e−18 ± 2.39e−19	99.08922 9.536e−16 ± 2.49e−18 6.032e−16 ± 2.60e−18	9.57062 7.704e−16 ± 3.11e−18 3.334e−16 ± 1.35e−17	⋯ 1.264e−15 ± 3.48e−18 1.269e−16 ± 6.08e−18	6.63e−17 ± 4.14e−19 1.070e−15 ± 4.69e−18 6.465e−17 ± 5.72e−18	1.02e−16 ± 1.79e−18 8.098e−16 ± 3.94e−18 1.372e−17 ± 3.79e−19
BSS2	3326786082988414592 1.239e−15 ± 8.11e−18 8.591e−16 ± 2.40e−18 6.725e−18 ± 1.55e−19	99.10026 1.096e−15 ± 2.83e−18 7.978e−16 ± 2.70e−18	9.48216 9.562e−16 ± 4.67e−18 4.594e−16 ± 2.71e−17	⋯ 1.301e−15 ± 3.86e−18 1.914e−16 ± 1.34e−17	5.71e−17 ± 3.85e−19 1.185e−15 ± 1.06e−18 7.975e−17 ± 7.27e−18	8.43e−17 ± 1.57e−18 1.010e−15 ± 4.17e−18 2.753e−17 ± 3.80e−19
BSS3	3326781238265313792 1.486e−15 ± 5.86e−18 1.155e−15 ± 3.36e−18 1.430e−17 ± 3.95e−19	99.15489 1.327e−15 ± 4.22e−18 1.104e−15 ± 5.40e−18	9.42449 1.285e−15 ± 5.24e−18 7.129e−16 ± 2.17e−17	⋯ 1.533e−15 ± 5.32e−18 3.422e−16 ± 1.26e−17	8.21e−17 ± 3.83e−19 1.457e−15 ± 4.07e−18 1.397e−16 ± 5.02e−18	⋯ 1.304e−15 ± 9.48e−18 3.690e−17 ± 8.16e−19
BSS4	3326786353568812416 2.038e−15 ± 9.53e−18 1.343e−15 ± 3.44e−18 6.719e−18 ± 9.90e−20	99.17258 1.759e−15 ± 5.19e−18 1.238e−15 ± 5.26e−18	9.50548 1.501e−15 ± 7.17e−18 7.122e−16 ± 1.71e−17	⋯ 2.203e−15 ± 9.72e−18 3.103e−16 ± 7.43e−18	2.09e−16 ± 7.11e−19 1.898e−15 ± 1.53e−17 1.445e−16 ± 7.19e−18	1.20e−16 ± 2.30e−18 1.571e−15 ± 1.91e−18 3.366e−17 ± 3.72e−19
BSS5	3326811096877800448 2.011e−15 ± 6.06e−18 1.375e−15 ± 3.01e−18 9.215e−18 ± 3.65e−19	99.18003 1.778e−15 ± 4.56e−18 1.261e−15 ± 3.97e−18	9.57457 1.530e−15 ± 5.87e−18 7.603e−16 ± 2.45e−17	⋯ 2.190e−15 ± 3.77e−18 3.463e−16 ± 9.57e−18	6.62e−17 ± 3.87e−19 1.930e−15 ± 4.24e−18 1.471e−16 ± 6.23e−18	1.57e−16 ± 2.01e−18 1.616e−15 ± 3.39e−18 3.323e−17 ± 7.96e−19
BSS6	3326779726436867456 3.732e−15 ± 1.16e−17 3.190e−15 ± 5.44e−18 2.296e−17 ± 5.71e−19	99.19927 3.577e−15 ± 9.14e−18 3.091e−15 ± 1.21e−17	9.34471 3.365e−15 ± 1.20e−17 1.905e−15 ± 4.56e−17	⋯ 3.861e−15 ± 5.64e−18 8.746e−16 ± 1.85e−17	1.071e−16 ± 4.37e−19 3.838e−15 ± 4.32e−18 3.796e−16 ± 1.12e−17	1.160e−16 ± 1.68e−18 3.466e−15 ± 5.41e−18 7.696e−17 ± 1.77e−18
BSS7	3326786426585687040 3.498e−15 ± 9.81e−18 2.271e−15 ± 5.72e−18 1.535e−17 ± 5.66e−19	99.20454 3.024e−15 ± 7.74e−18 2.067e−15 ± 4.89e−18	9.50730 2.551e−15 ± 9.18e−18 1.251e−15 ± 4.15e−17	2.044e−16 ± 1.03e−18 3.783e−15 ± 6.33e−18 5.408e−16 ± 2.04e−17	2.075e−16 ± 7.56e−19 3.291e−15 ± 6.13e−18 2.279e−16 ± 7.77e−18	2.750e−16 ± 2.70e−18 2.660e−15 ± 3.16e−18 5.606e−17 ± 1.70e−18
BSS8	3326782303417071104 1.056e−15 ± 7.09e−18 5.890e−16 ± 1.48e−18 3.091e−18 ± 2.48e−19	99.27360 8.599e−16 ± 2.25e−18 5.391e−16 ± 1.64e−18	9.46004 6.962e−16 ± 5.35e−18 3.086e−16 ± 1.42e−17	6.892e−17 ± 4.22e−19 1.184e−15 ± 1.10e−17 1.317e−16 ± 8.61e−18	⋯ 9.424e−16 ± 4.11e−18 6.927e−17 ± 6.57e−18	1.110e−16 ± 2.48e−18 7.362e−16 ± 2.02e−18 1.155e−17 ± 3.94e−19
BSS9	3326810478402457088 1.379e−15 ± 4.88e−18 8.496e−16 ± 4.70e−18 5.078e−18 ± 2.48e−19	99.28002 1.176e−15 ± 3.04e−18 7.752e−16 ± 3.34e−18	9.56600 9.679e−16 ± 3.99e−18 4.552e−16 ± 1.68e−17	7.950e−17 ± 4.72e−19 1.547e−15 ± 5.21e−18 2.006e−16 ± 1.05e−17	⋯ 1.310e−15 ± 4.35e−18 9.123e−17 ± 6.47e−18	1.360e−16 ± 1.90e−18 1.037e−15 ± 1.77e−18 1.958e−17 ± 5.77e−19
BSS10	3326792680058027776 1.697e−15 ± 6.11e−18 1.013e−15 ± 2.30e−18 6.323e−18 ± 2.74e−19	99.37616 1.421e−15 ± 3.65e−18 9.292e−16 ± 3.76e−18	9.40939 1.162e−15 ± 4.61e−18 5.393e−16 ± 1.99e−17	8.701e−17 ± 4.95e−19 1.893e−15 ± 6.32e−18 2.472e−16 ± 7.97e−18	⋯ 1.562e−15 ± 4.86e−18 9.921e−17 ± 6.21e−18	⋯ 1.234e−15 ± 2.78e−18 2.128e−17 ± 5.88e−19

Note. All flux measurements are provided in units of erg s^{-1} cm^{-2} $Å^{-1}$.

Table 4
Source IDs from Gaia DR3, along with the Coordinates, Flux Values, and Associated Flux Errors for the Stars across All Utilized Filters

Name	GAIA DR3 source_id GAIA3.Gbp ± err PS1.z ± err WISE.W2 ± err	R.A.(J2000) GAIA3.G ± err PS1.y ± err	Decl.(J2000) GAIA3.Grp ± err 2MASS.J ± err	F148W ± err PS1.g ± err 2MASS.H ± err	F154W ± err PS1.r ± err 2MASS.Ks ± err	GALEX.NUV ± err PS1.i ± err WISE.W1 ± err
BL1	3326773576044690048 5.233e−16 ± 3.286e−18 8.508e−16 ± 2.577e−19 1.043e−18 ± 7.202e−20	99.082557747051 7.437e−16 ± 2.640e−19 8.136e−16 ± 9.929e−19	9.30852649163554 8.420e−16 ± 2.087e−18 7.541e−17 ± 1.049e−17	5.313e−17 ± 7.388e−19 5.279e−16 ± 1.261e−18 4.264e−17 ± 6.519e−18	… 7.779e−16 ± 5.766e−19 1.627e−17 ± 2.736e−19	… 8.655e−16 ± 2.374e−19 4.073e−18 ± 8.628e−20
BL2	3326773095007479552 $5.895 \times 10^{-16} \pm 4.610 \times 10^{-18}$ $7.804 \times 10^{-16} \pm 1.505 \times 10^{-18}$ $1.019 \times 10^{-17} \pm 3.754 \times 10^{-19}$	99.0887354932615 $7.072 \times 10^{-16} \pm 1.859 \times 10^{-18}$ $7.623 \times 10^{-16} \pm 3.102 \times 10^{-18}$	9.26291017264503 $7.844 \times 10^{-16} \pm 3.625 \times 10^{-18}$ $5.636 \times 10^{-16} \pm 2.700 \times 10^{-17}$	… $5.481 \times 10^{-16} \pm 1.342 \times 10^{-18}$ $3.235 \times 10^{-16} \pm 1.549 \times 10^{-17}$	3.301e−17 ± 5.057e−19 $7.533 \times 10^{-16} \pm 2.583 \times 10^{-18}$ $1.482 \times 10^{-16} \pm 8.055 \times 10^{-18}$	… $8.078 \times 10^{-16} \pm 1.704 \times 10^{-18}$ $3.657 \times 10^{-17} \pm 9.093 \times 10^{-19}$
BL3	… $1.182 \times 10^{-16} \pm 3.227 \times 10^{-18}$ $1.290 \times 10^{-16} \pm 8.410 \times 10^{-19}$ $1.352 \times 10^{-18} \pm 6.972 \times 10^{-20}$	99.1258005764721 $1.317 \times 10^{-16} \pm 4.038 \times 10^{-19}$ $1.210 \times 10^{-16} \pm 1.338 \times 10^{-18}$	9.68017881401414 $1.330 \times 10^{-16} \pm 1.481 \times 10^{-18}$ $7.362 \times 10^{-17} \pm 1.024 \times 10^{-17}$	5.416e−17 ± 7.539e−19 $1.254 \times 10^{-16} \pm 4.645 \times 10^{-19}$ $3.547 \times 10^{-17} \pm 6.403 \times 10^{-18}$	… $1.442 \times 10^{-16} \pm 8.090 \times 10^{-19}$ $1.567 \times 10^{-17} \pm 3.111 \times 10^{-18}$	… $1.397 \times 10^{-16} \pm 9.928 \times 10^{-19}$ $4.364 \times 10^{-18} \pm 9.245 \times 10^{-20}$
BL4	… $1.934 \times 10^{-16} \pm 2.627 \times 10^{-18}$ $2.079 \times 10^{-16} \pm 8.351 \times 10^{-19}$ $1.819 \times 10^{-18} \pm 3.534 \times 10^{-19}$	99.2157630812281 $2.070 \times 10^{-16} \pm 5.797 \times 10^{-19}$ $1.920 \times 10^{-16} \pm 6.574 \times 10^{-19}$	9.43928148726254 $2.139 \times 10^{-16} \pm 2.051 \times 10^{-18}$ $1.518 \times 10^{-16} \pm 1.105 \times 10^{-17}$	… $1.852 \times 10^{-16} \pm 1.425 \times 10^{-18}$ $7.262 \times 10^{-17} \pm 6.688 \times 10^{-18}$	1.838e−17 ± 2.723e−19 $2.245 \times 10^{-16} \pm 1.645 \times 10^{-18}$ $3.055 \times 10^{-17} \pm 5.880 \times 10^{-18}$	… $2.223 \times 10^{-16} \pm 8.594 \times 10^{-19}$ $9.653 \times 10^{-18} \pm 9.602 \times 10^{-19}$
BL5	… $2.278 \times 10^{-16} \pm 2.906 \times 10^{-18}$ $2.962 \times 10^{-16} \pm 7.721 \times 10^{-19}$ $3.389 \times 10^{-18} \pm 7.492 \times 10^{-20}$	99.2601107911937 $2.683 \times 10^{-16} \pm 7.484 \times 10^{-19}$ $2.855 \times 10^{-16} \pm 1.137 \times 10^{-18}$	9.32285864096568 $2.906 \times 10^{-16} \pm 2.056 \times 10^{-18}$ $2.035 \times 10^{-16} \pm 1.162 \times 10^{-17}$	4.370e−17 ± 5.740e−19 $2.139 \times 10^{-16} \pm 1.633 \times 10^{-18}$ $1.078 \times 10^{-16} \pm 7.347 \times 10^{-18}$	… $2.831 \times 10^{-16} \pm 2.072 \times 10^{-18}$ $4.670 \times 10^{-17} \pm 5.979 \times 10^{-18}$	… $3.051 \times 10^{-16} \pm 1.109 \times 10^{-18}$ $1.149 \times 10^{-17} \pm 1.905 \times 10^{-19}$
BL6	… $1.220 \times 10^{-16} \pm 3.354 \times 10^{-18}$ $1.471 \times 10^{-16} \pm 7.047 \times 10^{-19}$ $7.967 \times 10^{-19} \pm 5.871 \times 10^{-20}$	99.2609571545268 $1.391 \times 10^{-16} \pm 4.202 \times 10^{-19}$ $1.396 \times 10^{-16} \pm 1.161 \times 10^{-18}$	9.2673787689024 $1.480 \times 10^{-16} \pm 2.231 \times 10^{-18}$ $9.243 \times 10^{-17} \pm 9.634 \times 10^{-18}$	… $1.155 \times 10^{-16} \pm 8.356 \times 10^{-19}$ $5.642 \times 10^{-17} \pm 6.340 \times 10^{-18}$	3.419e−17 ± 4.751e−19 $1.482 \times 10^{-16} \pm 1.131 \times 10^{-18}$ $2.827 \times 10^{-17} \pm 5.130 \times 10^{-18}$	… $1.580 \times 10^{-16} \pm 5.478 \times 10^{-19}$ $4.511 \times 10^{-18} \pm 9.556 \times 10^{-20}$

Note. All flux measurements are provided in units of erg s^{-1} cm^{-2} $Å^{-1}$.

Table 5
The Estimated Parameters of the BSS and BL Candidates Using Best-fitted SEDs

Name	Component	log g	$N_{\rm fit}/N_{\rm tot}$	vgf_b	Temperature (K)	Radius ($R_\odot$)	Luminosity ($L_\odot$)
BSS1	single	3.0	0.76	7.38	9000 ± 125	1.56 ± 0.23	14.50 ± 4.29
BSS2	single	4.5	0.87	4.20	9250 ± 125	1.14 ± 0.11	26.27 ± 7.77
BSS3	single	3.0	0.69	0.29	8500 ± 125	2.46 ± 0.36	28.65 ± 8.46
	double	3.5	0.81	0.61	$31{,}000^{+3000}_{-1000}$	0.12 ± 0.02	$12.4^{+11.89}_{-5.83}$
BSS4	single	4.5	0.87	1.63	10,500 ± 125	2.13 ± 0.31	49.82 ± 14.71
BSS5	single	4.0	0.88	0.44	9000 ± 125	2.44 ± 0.36	35.03 ± 10.35
BSS6	single	4.0	0.88	0.40	9000 ± 125	3.62 ± 0.53	77.11 ± 22.78
BSS7	single	4.0	0.88	2.22	9250 ± 125	2.85 ± 0.42	59.50 ± 17.58
BSS8	single	4.5	0.88	0.60	9000 ± 125	1.38 ± 0.20	11.43 ± 3.38
BSS9	single	3.0	0.88	0.61	9250 ± 125	1.83 ± 0.27	22.21 ± 6.56
BSS10	single	4.0	0.87	0.16	9000 ± 125	1.92 ± 0.28	21.97 ± 6.49
BL1	single	3.5	0.93	9.55	6000 ± 125	0.98 ± 0.14	2.61 ± 0.78
BL2	single	4.0	0.87	7.89	6500 ± 125	2.73 ± 0.40	13.04 ± 3.86
	double	4.0	0.87	0.53	$39{,}000^{+3000}_{-1000}$	0.06 ± 0.01	$6.76^{+5.62}_{-3.08}$
BL3	single	4.0	0.93	9.69	6500 ± 125	0.94 ± 0.14	1.85 ± 0.55
	double	4.0	0.93	1.07	$39{,}000^{+3000}_{-1000}$	0.03 ± 0.01	$2.10^{+1.75}_{-0.96}$
BL4	single	3.0	0.81	8.50	6500 ± 125	1.26 ± 0.18	2.77 ± 0.82
	double	3.5	0.81	0.46	$31{,}000^{+3000}_{-1000}$	0.04 ± 0.01	$1.08^{+1.04}_{-0.51}$
BL5	single	3.5	1.00	9.24	6500 ± 125	1.63 ± 0.24	5.43 ± 1.61
	double	4.0	1.00	0.78	$39{,}000^{+3000}_{-1000}$	0.05 ± 0.01	$6.1^{+5.08}_{-2.79}$
BL6	single	4.5	1.00	18.14	7000 ± 125	1.07 ± 0.16	3.41 ± 1.01

Additionally, we find 11 MS sources with FUV counterparts; these are likely BL candidates. None of the UV sources without a counterpart in ML-MOC cluster members cross-identified with the E. L. Hunt & S. Reffert (2023) members. Therefore, we check for any nearby contaminants for these 13 BSS and 11 BL candidates. Finally, we include 10 BSS and six BL candidates for our full analysis.

The cumulative radial distribution suggests that BSS, RGB, and MSTO stars are significantly more segregated than the low-mass stars. Low-mass stars are distributed more uniformly, occupying the outer regions, consistent with expectations from two-body relaxation processes. There is no significant difference in the segregation observed in the BSS population with respect to the RGB stars or the MSTO stars. This implies that the cluster is currently undergoing dynamical evolution. K. K. Rao et al. (2023) determined the area intercepted between the cumulative radial distributions of BSS and another massive reference population, $A^+_{\rm rh}$, to be +0.084 for this cluster. Based on a comparison of $A^+_{\rm rh}$ for the other 23 OCs, K. K. Rao et al. (2023) reported this cluster to be of intermediate dynamical age, which is consistent with our finding. M. J. Rain et al. (2021), on the other hand, classified Trumpler 5 as family *I* based on the segregation between RGB and BSS populations, with RGB populations appearing more centrally concentrated. Their finding clearly contradicts our results, as we do not find any noticeable difference in the segregation of the BSSs and RGB stars. K. K. Rao et al. (2023) also reported BSSs to be slightly more segregated than the RGB stars, as illustrated in their A^+ value, +0.084, but not the other way round, as demonstrated by M. J. Rain et al. (2021). This discrepancy between our classification and that of M. J. Rain et al. (2021) could be due to differences in datasets and methodologies of DR correction and BSS identification used. M. J. Rain et al. (2021) used Gaia DR2 data for membership determination, whereas our analysis use Gaia DR3 data, which provides greater astrometric precision and completeness. Moreover, M. J. Rain et al. (2021) determined DR by selecting red clump stars, derived the reddening law from a linear least-squares fit, and adopted a reference red clump point as the zero-point for correction. For each field star, they estimated the mean differential extinction and reddening from the three nearest red clump stars and applied these corrections to its color and magnitude. On the other hand, we use MS stars to correct the DR reddening as explained in Section 3.3.

The availability of UVIT data from AstroSat for the OC Trumpler 5 has provided a valuable opportunity to investigate the properties of BSS candidates and BL candidates. To characterize these populations, we utilized photometric observations from AstroSat/UVIT in the F148W and F154W filters. These UVIT data are complemented with broad multiwavelength data ranging from optical to IR, enabling a comprehensive study of their formation mechanism and the fundamental parameters of BSS candidates and BL candidates by analyzing their SEDs. Of the identified high-probability cluster members, 13 BSS candidates and 11 MS stars have counterparts in UVIT (refer to Figure 3(b)). In our study we analyzed 10 BSS candidates and six BL candidates that have complete photometric data ranging from UV to IR and have no nearby sources within 3″.

Out of the 10 BSS candidates analyzed, nine were successfully fitted with single-component SEDs. For these BSS, the effective temperatures range from 9000 to 10,500 K, radii from 1.38 $R_\odot$ to 3.62 $R_\odot$, and luminosities from 3.21 $L_\odot$ to 77.11 $L_\odot$. The absence of UV excess in their SEDs points toward a formation channel via stellar mergers, which is consistent with the expectation for dynamically evolved OCs. However, the possibility of formation through MT cannot be entirely ruled out. If the BSSs have WD companions that have cooled below ∼11,000 K, these companions may remain undetected in the FUV regime, due to the sensitivity of the detector, making it difficult to confirm the MT origin without

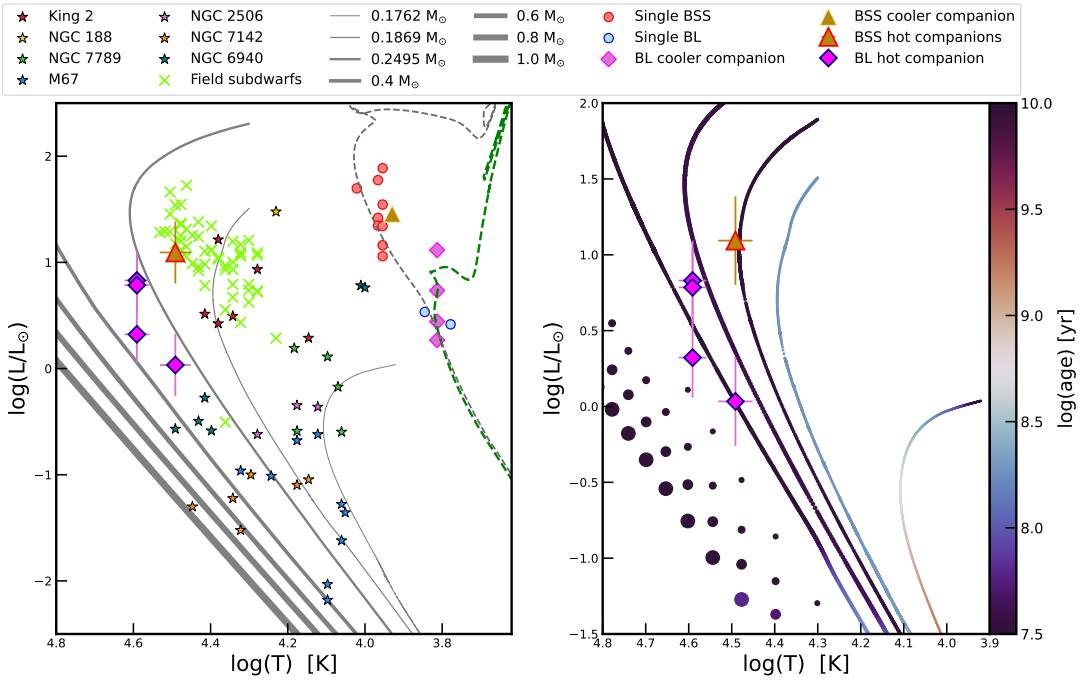

Figure 9. H-R diagram of Trumpler 5. The left panel contains a green dashed curve representing the PARSEC isochrone for an age of 3.0 Gyr, and the zero-age MS is depicted as a black dashed curve. Single-component BSS candidates are plotted as red solid circles, whereas the binary BSS is indicated by a yellow solid triangle. Single BL candidates are shown as blue filled circles, whereas binary BL candidates are plotted with magenta diamonds. The locations of field subdwarf stars from S. Geier (2020) are shown by green crosses. Binary-component stars from other OCs (King 2, NGC 188, NGC 2506, NGC 7142, NGC 7789, NGC 6940, and M67) are shown as star symbols in different colors, as indicated in the legend. Several solid gray curves represent cooling curves of WDs of different low and extremely low masses, sourced from J. A. Panei et al. (2007) and L. G. Althaus et al. (2013). The right panel highlights the hot companion of BSS3 and four BL candidates, placing them on the appropriate WD cooling track to estimate its approximate cooling age.

further spectroscopic evidence. Therefore, these BSSs may have formed either via Case-A MT or a merger in a triple system, or via Case-B/Case-C MT, and may have a cool WD as a companion that is below the detection limit of UVIT. For example, in BSS4, which is a known eclipsing binary in the Gaia DR2 catalog (refer to Figure 3(b)), we do not find any UV excess, hence we classify it as a single star. It is possible that the system may have a cool WD companion that is below the detection limit of the UVIT detector. We need spectroscopic observations to understand the formation mechanisms of these single-SED BSSs. We would also like to note that, for Trumpler 5, the issue of significant DR may have affected our SED fitting despite the careful analysis performed to estimate the value of extinction for each individual BSS. If the value of extinction is underestimated, the star may appear to have more UV excess, giving a false positive and suggesting a possible binary component. On the other hand, if extinction is overestimated, the star may appear to have less UV excess than the actual excess, and a real companion may be missed. For individual cases where both single and binary SED fitting are plausible, we have favored single SED fits for objects. The intrinsic limitations in any of the available methods, including the one used in our analysis to estimate the DR, can only be circumvented by spectroscopic observations of these objects. In Trumpler 5, we find a single BSS (BSS3) out of the 10 BSSs (10%) considered for SED analysis, with only UV excess greater than 50% compared to the fitted single Kurucz model. This is considerably lower than for other OCs studied under the UVIT Open Cluster Survey, where about 20%−60% of BSSs are suggested to have possibly formed via MT, and an even larger fraction are found with UV excess.

A single BSS candidate (BSS3) shows a significant UV excess, with fractional residual greater than 0.5. The best-fit binary SED model for BSS3 suggests the presence of a hot companion with an effective temperature of $31{,}000^{+3000}_{-1000}$ K, a radius of $0.05 \pm 0.01\ R_{\odot}$, and a luminosity of $0.06 \pm 0.02\ L_{\odot}$. Figure 9 shows the location of the hot companion of BSS3 in the H-R diagram. The hot companion lies in the same region occupied by field subdwarfs (S. Geier 2020; green crosses in Figure 9). The derived ranges of temperature and luminosity suggest that the companion is possibly a B-type subdwarf (sdB) star. This suggests that this BSS may have formed via Case-A/Case-B binary MT.

The sdB stars are core-helium-burning stars with a thin hydrogen envelope, with high effective temperatures ranging from ∼20,000 to 40,000 K for sdB and up to ∼80,000 K for sdO stars, $\log g \gtrsim 5.0$ (U. Heber 2016), and a mass around 0.5 $M_{\odot}$. The sdB stars may form via a stable Roche lobe overflow process in which the primary fills its Roche lobe while in its RGB phase and transfers the envelope to the companion; the stripped core is called the sdB star. In this MT, the companion may gain mass if the MT is conservative and appear as a BSS as a result of rejuvenation if the progenitor is already massive enough. However, observationally, the companions of sdB stars are, in most cases, found to be either WDs or low-mass M dwarfs in close orbits. Most binary population synthesis models (Z. Han et al. 2002; D. Clausen & R. A. Wade 2011) also predict that MT in the formation of sdB stars is nonconservative. The finding of an sdB star as a companion to BSS3 is therefore interesting, as such systems are rarely reported in the literature. V. V. Jadhav et al. (2021) reported sdB companions to six of the BSSs in the OC King 2.

BLs are thought to represent the low-luminosity counterparts of BSSs, primarily formed through binary interaction processes. They are typically marginally fainter than the MSTO, or distributed along the MS. Current formation scenarios suggest that BLs may arise from nonconservative MT, angular momentum loss in close binaries, or mergers that leave behind low-luminosity products compared to classical BSSs (E. M. Leiner et al. 2025). Their underlying nature is often inferred from indirect signatures such as UV excess emission, unusually high rotational velocities, or evidence of ongoing binary evolution. In our study, we identify six MS stars exhibiting significant UV counterparts in the UVIT filters F148W and F154W, which we classify as potential BL candidates. While their optical photometric properties are consistent with ordinary MS stars, the presence of a marked UV excess strongly suggests the possibility of an unresolved hot companion. Alternative explanations, however, such as enhanced chromospheric activity, rapid stellar rotation, or residual accretion cannot be excluded.

Of the six BL candidates, four are reasonably well fitted with binary-component SED models. The remaining two candidates (BL1 and BL6) could not be fitted satisfactorily with the available binary-component fit models. Confirming their true nature will require dedicated spectroscopic observations and time-series photometric monitoring. The hot companions of the four BL candidates have estimated effective temperatures ranging from 31,000 to 39,000 K, radii from 0.03 to 0.06 $R_{\odot}$, and luminosities from 1.08 to 6.76 $L_{\odot}$. Their positions in the H-R diagram coincide with regions populated by WD cooling curves of mass 0.24 $M_{\odot}$ to 0.4 $M_{\odot}$ (J. A. Panei et al. 2007), suggesting that the companions are low-mass WDs. Such low-mass WD companions favor a Case-A/Case-B MT origin for BSSs, since such objects cannot be formed through single-star evolution within the Hubble time (J. M. Brown et al. 2011). Therefore, this gives evidence that these BL candidates have formed via an MT process. For reference, the positions of the hot companions of BSSs and BLs of other OCs (A. Subramaniam et al. 2016; N. Sindhu et al. 2019; S. Geier 2020; V. V. Jadhav et al. 2021; A. Panthi et al. 2022, 2024; K. Vaidya et al. 2022; A. Panthi & K. Vaidya 2024) are shown on the left panel of Figure 9. The right panel of Figure 9 shows the approximate ages of the hot companions of BSSs and BLs. The BSSs and four BL candidates have formed very recently, having undergone the MT process ∼155 Myr and 26–38 Myr ago, respectively. High-resolution spectroscopic data and time-series radial velocity measurements will be essential to confirm the nature of hot companions in the future.

5. Conclusion

The main findings of our study are summarized below.

1. We analyzed the old OC Trumpler 5 using multi-wavelength data, including AstroSat/UVIT observations, to characterize its stellar population and investigate the BSS and BL candidates. Cluster membership was determined using ML-MOC, and a total of 3150 high-probability members and an additional 305 moderate-probability members were obtained. Given the high and nonuniform extinction across the cluster, we applied DR correction, resulting in a cleaner and accurate CMD.
2. A total of 13 BSS candidates and 11 MS stars have counterparts in UVIT. However, we focused on 10 BSS and six BL candidates for which complete photometric data from UV to IR were available. Among these, nine BSSs were successfully fitted with single-component SEDs, exhibiting temperatures between 9000 and 10,500 K, radii between 1.38 and 3.62 $R_{\odot}$, and luminosities between 11.43 and 77.11 $L_{\odot}$. These parameters suggest a likely formation through stellar mergers. However, formation via MT cannot be entirely ruled out, especially if the BSSs have WD companions that have cooled below ∼11,000 K.
3. One BSS candidate, BSS3, showed significant UV excess with fractional residual greater than 0.5, indicating the presence of an unresolved hot companion. This star was successfully fitted with a binary-component SED, supporting the MT formation mechanism. The temperature and luminosity range of the hot companion suggest that it may be an sdB star. The hot companion was found to have an effective temperature of 31,000 K and a luminosity of 0.06 $L_{\odot}$, consistent with the properties of an sdB star. BSS3 has formed very recently via Case-A/Case-B MT and has an age of ∼155 Myr.
4. BL1 and BL6 showed significant UV excess, but could not be satisfactorily fitted with binary-component SEDs, therefore we present their single-SED fits only and their nature remains inconclusive.
5. Of the six BL candidates, four fitted well with binary-component SED models, indicating the presence of hot companions. The derived properties of the hot companions of the four BL candidates are consistent with low-mass WD stars. The BLs have formed very recently via Case-A/Case-B MT and their ages range from ∼26 to 38 Myr.

Acknowledgments

We thank the anonymous referee for valuable comments and suggestions, which have significantly improved the quality of this paper. The authors also acknowledge Manan Agarwal for developing the ML-MOC algorithm used to determine cluster membership in this study. The authors also gratefully acknowledge discussions with Dr. Khushboo K. Rao on the method of differential reddening estimation. This work uses the data from UVIT on board AstroSat mission of Indian Space Research Organisation (ISRO). UVIT is a collaborative project between the Indian Institute of Astrophysics (IIA), Bengaluru; the Inter-University Centre for Astronomy and Astrophysics (IUCAA), Pune; the Tata Institute of Fundamental Research (TIFR), Mumbai; several centers of the Indian Space Research Organisation (ISRO); and the Canadian Space Agency (CSA). This work has made use of data from the third data release of the European Space Agency (ESA) mission Gaia (https://www.cosmos.esa.int/gaia), Gaia DR3 (A. Vallenari et al. 2023), processed by the Gaia Data Processing and Analysis Consortium (DPAC; https://www.cosmos.esa.int/web/gaia/dpac/consortium). This research made use of the Astropy Python package for astronomy (Astropy Collaboration et al. 2013), NumPy (C. R. Harris et al. 2020), and Matplotlib (J. Hunter 2007). We also acknowledge the use of NASA's Astrophysics Data System (ADS; https://ui.adsabs.harvard.edu).

Data Availability

The data underlying this article are publicly available at https://gea.esac.esa.int/archive. The ML-MOC algorithm-derived membership probabilities are available as the data behind Figure 1. The derived data generated in this research will be shared upon reasonable request to the corresponding author.

ORCID iDs

Komal Chand https://orcid.org/0009-0008-0887-6636
Anju Panthi https://orcid.org/0009-0003-3930-2778

References

Agarwal, M., Rao, K. K., Vaidya, K., & Bhattacharya, S. 2021, MNRAS, 502, 2582
Agrawal, P. C. 2017, JApA, 38, 27
Alessandrini, E., Lanzoni, B., Ferraro, F. R., Miocchi, P., & Vesperini, E. 2016, ApJ, 833, 252
Althaus, L. G., Bertolami, M. M. M., & Córsico, A. H. 2013, A&A, 557, A19
Astropy Collaboration, Robitaille, T. P., Tollerud, E. J., et al. 2013, A&A, 558, A33
Aurière, M., Ortolani, S., & Lauzeral, C. 1990, Natur, 344, 638
Bailer-Jones, C., Rybizki, J., Fouesneau, M., Demleitner, M., & Andrae, R. 2021, yCat, 1352, 0
Bayo, A., Rodrigo, C., Barrado Y Navascués, D., et al. 2008, A&A, 492, 277
Boffin, H. M., Carraro, G., Beccari, G., et al. 2015, Ecology of Blue Straggler Stars, Vol. 413 (Springer)
Bressan, A., Marigo, P., Girardi, L., et al. 2012, MNRAS, 427, 127
Brown, J. M., Kilic, M., Brown, W. R., & Kenyon, S. J. 2011, ApJ, 730, 67
Cantat-Gaudin, T., Fouesneau, M., Rix, H.-W., et al. 2023, A&A, 669, A55
Cassarà, L. P., Piovan, L., Weiss, A., Salaris, M., & Chiosi, C. 2013, MNRAS, 436, 2824
Castelli, F., Gratton, R., & Kurucz, R. 1997, A&A, 318, 841
Chand, K., Kunwar Rao, K., Vaidya, K., & Panthi, A. 2024, BSRSL, 93, 262
Chen, X., & Han, Z. 2008, MNRAS, 387, 1416
Clausen, D., & Wade, R. A. 2011, ApJL, 733, L42
Cohen, M., Wheaton, W. A., & Megeath, S. 2003, AJ, 126, 1090
Cover, T., & Hart, P. 1967, ITIT, 13, 21
Ferraro, F. R., & Lanzoni, B. 2007, IAU, 14, 438
Fiorentino, G., Lanzoni, B., Dalessandro, E., et al. 2014, ApJ, 783, 34
Fitzpatrick, E. L. 1999, PASP, 111, 63
Friel, E. D. 2013, in Planets, Stars and Stellar Systems. Volume 5: Galactic Structure and Stellar Populations, ed. T. D. Oswalt & G. Gilmore, Vol. 5 (Springer), 347
Geier, S. 2020, A&A, 635, A193
Geller, A. M., & Mathieu, R. D. 2011, Natur, 478, 356
Gosnell, N. M., Mathieu, R. D., Geller, A. M., et al. 2015, ApJ, 814, 163
Green, G. M., Schlafly, E., Zucker, C., Speagle, J. S., & Finkbeiner, D. 2019, ApJ, 887, 93
Han, Z., Podsiadlowski, P., Maxted, P. F., Marsh, T. R., & Ivanova, N. 2002, MNRAS, 336, 449
Harris, C. R., Millman, K. J., Van Der Walt, S. J., et al. 2020, Natur, 585, 357
Heber, U. 2016, PASP, 128, 082001
Hills, J., & Day, C. 1976, ApL, 17, 87
Hunt, E. L., & Reffert, S. 2023, A&A, 673, A114
Hunter, J. 2007, CSE, 9, 90
Indebetouw, R., Mathis, J., Babler, B., et al. 2005, ApJ, 619, 931
Jadhav, V. V., Pandey, S., Subramaniam, A., & Sagar, R. 2021, JApA, 42, 89
Jadhav, V. V., Pennock, C. M., Subramaniam, A., Sagar, R., & Nayak, P. K. 2021, MNRAS, 503, 236
Jadhav, V. V., Sindhu, N., & Subramaniam, A. 2019, ApJ, 886, 13
Jordi, C., Gebran, M., Carrasco, J., et al. 2010, A&A, 523, A48
Kumar, A., Ghosh, S. K., Hutchings, J., et al. 2012, SPIE, 8443, 84431N
Leiner, E., Mathieu, R. D., Vanderburg, A., Gosnell, N. M., & Smith, J. C. 2019, ApJ, 881, 47
Leiner, E. M., Gosnell, N. M., Geller, A. M., et al. 2025, ApJL, 979, L1
Leonard, P. J. 1996, ApJ, 470, 521
Lucertini, F., Monaco, L., Caffau, E., et al. 2023, A&A, 671, A137
Martin, D. C., Fanson, J., Schiminovich, D., et al. 2005, ApJL, 619, L1
Massari, D., Mucciarelli, A., Dalessandro, E., et al. 2012, ApJL, 755, L32
McCrea, W. 1964, MNRAS, 128, 147
Meylan, G., & Heggie, D. C. 1997, A&ARv, 8, 1
Milone, A. P., Piotto, G., Bedin, L. R., et al. 2012, A&A, 540, A16
Panei, J. A., Althaus, L. G., Chen, X., & Han, Z. 2007, MNRAS, 382, 779
Panthi, A., & Vaidya, K. 2024, MNRAS, 527, 10335
Panthi, A., Vaidya, K., Jadhav, V., et al. 2022, MNRAS, 516, 5318
Panthi, A., Vaidya, K., Vernekar, N., et al. 2024, MNRAS, 527, 8325
Peel, D., & McLachlan, G. J. 2000, Statistics and Computing, 10, 339
Perets, H. B., & Fabrycky, D. C. 2009, ApJ, 697, 1048
Piatti, A. E., Clariá, J. J., & Ahumada, A. V. 2004, MNRAS, 349, 641
Platais, I., Melo, C., Quinn, S., et al. 2012, ApJL, 751, L8
Postma, J. E., & Leahy, D. 2017, PASP, 129, 115002
Rain, M. J., Ahumada, J. A., & Carraro, G. 2021, A&A, 650, A67
Rao, K. K., Vaidya, K., Agarwal, M., Balan, S., & Bhattacharya, S. 2023, MNRAS, 526, 1057
Rao, K. K., Vaidya, K., Agarwal, M., & Bhattacharya, S. 2021, MNRAS, 508, 4919
Rao, K. K., Vaidya, K., Agarwal, M., et al. 2022, MNRAS, 516, 2444
Sandage, A. 1953, AJ, 58, 61
Schlafly, E., Finkbeiner, D., Jurić, M., et al. 2012, ApJ, 756, 158
Shara, M. M., Saffer, R. A., & Livio, M. 1997, ApJL, 489, L59
Sindhu, N., Subramaniam, A., Jadhav, V. V., et al. 2019, ApJ, 882, 43
Sindhu, N., Subramaniam, A., & Radha, C. A. 2018, MNRAS, 481, 226
Singh, K. P., Tandon, S. N., Agrawal, P. C., et al. 2014, SPIE, 9144, 91441S
Stetson, P. B. 1987, PASP, 99, 191
Subramaniam, A., Sindhu, N., Tandon, S. N., et al. 2016, ApJL, 833, L27
Tandon, S. N., Hutchings, J. B., Ghosh, S. K., et al. 2017, JApA, 38, 28
Tandon, S. N., Postma, J., Joseph, P., et al. 2020, AJ, 159, 158
Tonry, J., Stubbs, C. W., Lykke, K. R., et al. 2012, ApJ, 750, 99
Vaidya, K., Panthi, A., Agarwal, M., et al. 2022, MNRAS, 511, 2274
Vallenari, A., Brown, A. G., Prusti, T., et al. 2023, A&A, 674, A1
Wang, S., & Chen, X. 2019, ApJ, 877, 116
Webbink, R. F. 1976, ApJ, 209, 829
Wright, E. L., Eisenhardt, P. R., Mainzer, A. K., et al. 2010, AJ, 140, 1868